

# C<sub>s</sub>-corrected STEM imaging of both pure and Ag-supported metal-organic framework MIL-100(Fe)

Alvaro Mayoral, <sup>\*[a]</sup> Rubén Mahugo,<sup>[b]</sup> Manuel Sánchez-Sánchez,<sup>[b]</sup> Isabel Díaz<sup>[b]</sup>

**Abstract:** Metal-organic frameworks (MOFs) are a family of porous solids combining organic and inorganic moieties with tunable porosity. Their particular structural parameters have converted MOFs into suitable compounds for gas storage or drug delivery. However, despite the excellent crystallinity they tend to exhibit their analysis through transmission electron microscopy is extraordinarily complicated due to the high instability under the electron beam irradiation. In here, high-resolution C<sub>s</sub>-corrected STEM imaging has been used for the observation of the building units of MIL-100(Fe) paying special attention to the electron beam current. In addition, MIL-100(Fe) has been reacted with AgNO<sub>3</sub> through a solid-state reaction technique, which has resulted into the formation of metal nanoparticles on the surface. The incorporation of Ag into the porous network has been also investigated.

## Introduction

Metal-organic frameworks (MOFs) is a fairly recently new family of hybrid organic-inorganic crystalline porous solids with tunable porosity, structure, composition and properties; they can be generally described as metal ions or clusters connected by organic bridges to finally produce a bi- or three dimensional porous network<sup>[1]</sup>. MOFs can be prepared by a variety of methodologies which are continuously being explored with the intention of producing new materials under more economically demanded and sustainable circumstances<sup>[2]</sup>. Their extraordinary high surface areas, together with their structural features have converted MOFs materials into potential candidates for gas storage and conversion<sup>[3]</sup>, catalysis<sup>[2c, 4]</sup> or drug delivery<sup>[5]</sup>. In this sense, an advance and precise characterization of the MOF materials particularly that focused on their crystal growth, porous system, connectivity and crystallographic features becomes essential to evaluate the potential applications of MOF materials. Like in other porous frameworks, the crystallographic structures have been mainly studied by X-ray diffraction methods<sup>[6]</sup>. Despite the valuable information that can be extracted by means of this technique, there are numerous cases where additional structural knowledge needs to be acquired. Maybe the most evident example is the structural defects in MOFs (surfaces, interfaces, disorders, linker and/or metal vacancies, etc.), which are deliberately ignored by crystallographic techniques but can strongly affect the physicochemical properties of the material and their subsequent role/behavior in certain applications<sup>[7]</sup>.

In this context, transmission electron microscopy (TEM) can offer an elegant solution because, when combined with the electron diffraction and with the modern spherical aberration correctors atomic resolution data can be produced allowing a clear visualization of structural defects of inorganic solids<sup>[8]</sup>. This technique, especially after the implementation of the spherical aberration correctors<sup>[9]</sup>, has been of crucial importance on the development of material science in general and on the characterization of metals at atomic scale in particular<sup>[10]</sup>. In order to achieve such high-resolution and good signal-to-noise ratio images, the metallic nanoparticles tended to be deposited on lighter and stable supports allowing a strong beam current to be used. This mode of operation has resulted on the possibility of acquiring images of isolated metal atoms or even obtaining chemical information through spectroscopic analyses (which require high dose and longer exposure times). Unfortunately, a similar approach cannot be undertaken when the supports suffer from severe beam damage, as due to the interaction of the electron beam with the material, the structure of the host would collapse resulting on the agglomeration of the metals incorporated.

For the particular case of porous structures, there have been a high number of works dealing with the effect of the electron beam as it tend to quickly damage their framework<sup>[11]</sup>. Many aspects have been investigated in order to extend the lifetime of such beam sensitive materials under the electron beam, from reducing the accelerating voltage<sup>[12]</sup> to working under liquid nitrogen temperature<sup>[13]</sup>, although it has been recently proved that the most

---

[a] Dr. A. Mayoral  
Laboratorio de Microscopias Avanzadas (LMA), Nanoscience  
Institute of Aragon (INA)  
University of Zaragoza  
Mariano Esquillor, Edificio I+D, 50018, Zaragoza, Spain.  
E-mail: amayoral@unizar.es

[b] R. Mahugo, Dr. M. Sanchez-Sanchez, Dr. I. Diaz.  
Instituto de Catálisis y Petroleoquímica  
CSIC  
C/ Marie Curie 2, 28049 Madrid, Spain

Supporting information for this article is given via a link at the end of the document. **(Please delete this text if not appropriate)**

crucial factor is the electron dose that interact with the material. By a careful control of this parameter, both the beam current and the dwell time can be minimized and atomic resolution can be reached. This approach has been mainly undertaken in a spherical aberration ( $C_s$ -corrected) in Scanning Mode (STEM) using a High Angle Annular Dark Field (HAADF) detector when Z contrast was necessary<sup>[8c, 14]</sup> or an Annular Dark Field Detector (ADF) when it was intended to increase the signal to noise ratio<sup>[15]</sup> while minimizing the electron dose, or even a combination of both<sup>[16]</sup>. This kind of studies on MOFs materials are scarcer due to their higher beam sensitivity compared to zeolites although in the last years impressive results on the framework observation are being achieved through  $C_s$ -corrected STEM and TEM<sup>[2c, 2d, 15a, 17]</sup>. Another great advantage of electron microscopy compared with other characterization methods consists in the ability of imaging guest species incorporated onto the porous system of the MOFs<sup>[17a, 18]</sup>. This characteristic would be of crucial interest in order to develop functional materials with controllable porosity and tunable properties coming from the metallic nanoparticles incorporated into the frameworks. The major difficulties that one could encounter in comparison with metals supported in other more stable supports<sup>[19]</sup> would be retaining the porous structure while obtaining enough signal-to-noise ratio images that allow identifying the guest species.

In the present work we have intended to obtain ultrahigh resolution images of the widely-investigated MOF MIL-100(Fe) that has a cubic arrangement of mesocages making more complicated its image interpretation due to the large number of atoms on the projected image. In addition, silver species have been attempted to be supported either outside of the crystals or into the cavities and observed by  $C_s$ -corrected STEM analysis.

## Results and Discussion

MIL-100(Fe) crystals tend to exhibit faceted morphology where in many cases structural defects such as twin planes can be found. Figure 1a exhibits the low-magnification image of a structural defect in a MIL-100 crystal. A closer look of the twin plane (forming an angle of  $130^\circ$ ) is shown inset. The crystal structure consists of a cubic system with  $Fd-3m$  space group and lattice constants  $a = b = c = 73.34 \text{ \AA}$ <sup>[20]</sup>. The structure has been described as an iron carboxylate where iron octahedra are linked through sharing a common vertex  $\mu_3\text{-O}$  forming trimers. Figure 1b displays the schematic representation of the material orientated along the  $[110]$  zone axis, presenting a  $2\text{-fold}$  symmetry, where the iron cations are represented as red octahedra, while the carbon appears in blue (for simplicity oxygen atoms have been omitted). Due to the low stability of ordered porous materials in general and MOF in particular, obtaining high resolution images of the framework has been extraordinary difficult minimizing the spatial resolution that can be achieved. Therefore imaging these materials have been the result of a compromise between number of electrons and enough signal-to-noise ratio. If low-dose technique are applied images are virtually inexistent due to the high amount of noise; on the contrary, if the beam current is increased the material becomes irreversibly damaged giving no information of the structure. By using an ADF (Annular Dark Field) detector the signal to noise ratio can be increased in comparison with the pure HAADF mode of operation, facilitating the reduction of the electron dose in order to reduce the beam damage. In the former mode the inner collection angle is smaller than for HAADF mode, 15 mrad versus 70 mrad, collecting more electrons and therefore increasing the contrast of the experimental images. This technique is particularly useful to image crystalline frameworks, including even the location of light compounds<sup>[2c, 15a, 16-17, 21]</sup>. Although it is still a dark field image affected by the atomic number, it is less affected by this parameter than for the HAADF case as it contains more diffraction effects.

Figure 2 presents the  $C_s$ -corrected images of MIL-100(Fe) along the  $[110]$  zone axis. Figures 2a and 2b correspond to the simultaneously recorded high-magnification images of MIL-100(Fe) using two detectors situated at different positions which allowed recording pure HAADF data (Figure 2a) and ADF data (Figure 2b). Both images were recorded over  $6 \mu\text{s}$  per pixel using an image resolution of  $1024 \times 1024$  pixels giving a pixel size in this case of  $0.068 \text{ nm} \times 0.068 \text{ nm}$  and the beam current was set to  $2 \text{ pA}$ . The signal to noise ratio is very low in Figure 2a, which was registered using a detector with an inner angle of 70 mrad. The Fast Fourier Transform (FFT) extracted from this image is shown in Figure 2c. It indicates an information transfer of  $8.10 \text{ \AA}$ . Under the same conditions but using a dark field detector (15 mrad inner angle) the image contains clearer features with a better contrast giving an information transfer of  $5.63 \text{ \AA}$  (Figure 2d) and the measured unit cell assuming  $Fd-3m$  symmetry was  $a = b = c = 71.54 \text{ \AA}$ . The reasons behind the slight underestimation of the cell parameters by this technique in comparison with those giving by X-ray crystallographic solving, are discussed elsewhere<sup>[2c, 15a]</sup>.

With the intention of gaining better contrast and in order to improve image resolution, images were FFT filtered (Figure 3). Figures 3a and 3b show a HAADF and an ADF images respectively, giving a clearer image of the framework. Still, due to the high complexity of this framework that contains a great number of atoms on the projected image (as depicted in the model from Figure 1b) where heavier elements such as Fe is connected through lighter ones, C, O and H, image interpretation is more complex compared to those of the other MOF frameworks<sup>[15a, 17b]</sup>, where empty channels can be clearly visualized. In addition, the fact that the unit cell is

significantly smaller than that of the MIL-101 material, also studied by this approach elsewhere<sup>[17a]</sup>, makes that our study requires higher magnification image recording resulting in a faster beam damage of the material. By analysing the raw images along the [110] through CRISP software<sup>[22]</sup>, the lattice was refined using the (1-11) and the (-111) reflections and the electrostatic projected potential maps can be obtained by imposing  $P2$  symmetry (Figures 3c and 3d for HAADF and ADF respectively). Despite the weak signal obtained for the HAADF data the extracted potential map allows a clear visualization of the structure similar to the data obtained by ADF imaging suggesting that still lower beam current could be employed in order to record high-resolution images while preserving the framework structure intact. The model, where Fe appears as red spheres and C appears in blue, has been superimposed for better understanding of the images obtained and to corroborate the high quality of the data reported. Figures 3e and 3f show a magnified region of the image and of the model where the iron trimers that lead into the formation of the so-called supertetrahedra are marked by orange circles. Many of the potential applications of metal organic frameworks rely on their capability to act as host of different metals, which can provide properties additional to the intrinsic ones due to their porous nature<sup>[23]</sup>. Silver has been attempted to be introduced in MIL-100 through a simple method based on a solid-state reaction. The intention was to generate both external  $\text{Ag}^0$  (nano)particles or nanoclusters of  $\text{Ag}^0$  within the MIL-100(Fe) cavities.  $\text{AgNO}_3$  was deeply mixed with MIL-100(Fe) using a mortar and pestle in a similar manner as it has been done for zeolites<sup>[24]</sup> and heated up to 150 °C for 12 hours. Under these conditions, the Ag species resulted mainly reduced to  $\text{Ag}^0$  according to the powder XRD patterns (Figure 4) due to the spontaneous reduction of  $\text{Ag}^+$  to  $\text{Ag}^0$  as observed in some other MOFs<sup>[25]</sup>.

Three different Ag loadings were studied based on the Fe to Ag molar ratios being 10:1, 5:1 and 1:1 Fe:Ag. In every case the MIL-100(Fe) structure was preserved regardless of the  $\text{AgNO}_3$  amount. Even though we are working well below the  $\text{AgNO}_3$  melting point it seems that the MIL-100(Fe), probably due to water content inside the pores, act as a solvent as no silver nanoparticles were found separated from the MOF crystallites, suggesting that the salt may penetrate through the porous network to some extent to finally diffuse through the cavities onto the outer surface growing the metal nanoparticles. The XRD analyses (Figures 4a and 4b) and the  $\text{N}_2$  isotherms and pore size distribution (Figures S1 and S2 and Table S1) corroborated the good crystallinity of the MIL-100(Fe) after being reacted as well as the increment of the diffraction peaks corresponding to  $\text{Ag}^0$  when the amount of salt was increased (denoted by asterisks in Figure 4a). Interestingly, this simple loading method has yielded highly dispersed metal particles supported on the surface of MOF crystals. Low-magnification images depicted in Figures 4c, 4d and 4e illustrated the presence of silver nanoparticles on the surface of the MIL-100(Fe). From these images it can be concluded that lots of silver is coating the surface of the porous material for 1:1 Fe:Ag sample forming larger aggregates of metal marked by red circles. The presence of silver particles obviously decreases in the 5:1 sample observing even smaller dispersed  $\text{Ag}^0$  particles. However, it is of particular interest the material with lower amount of Ag, 10:1 Fe:Ag, shown in Figure 4e, in which very small (< 8 nm) and homogeneous particles are observed, dispersed on the surface of the MIL-100(Fe). This effect is rather remarkable since there is no charge in the MOF framework that may drive the uptake of silver such as the case of zeolites, in which the cation exchange triggers the metal loading. A closer look to the low angle X-ray diffraction patterns shows the inversion of the relative intensities of the 220 and 311 reflections upon loading<sup>[24]</sup> (Figure 4b). As we mentioned earlier, the diffusion of the silver salt could be explained by the presence of the water inside the MOF that, while temperature increases, releases it back in a controlled manner due to the porous network yielding the formation of small  $\text{Ag}^0$  nanoparticles.

A closer inspection of areas with less density of Ag suggests that some metal may go inside the pores. Figure 5a corresponds to a MIL-100(Fe) orientated along the [110] direction where cavities can be identified. The material with the same  $Fd-3m$  symmetry than the parental MIL-100 presented a unit cell value of  $a = 70.69 \text{ \AA}$ , maintaining the same lattice constants as the Ag-free MIL-100(Fe). In this case a different contrast can be observed pointed by red arrows in Figure 5b. These images were recorded using a beam current of 2 pA, with a dwell time of 6  $\mu\text{s}$  per pixel and a  $1024 \times 1024$  pixels per image. In this case the micrograph shown in Figure 5b was recorded right after Figure 5a and although it is possible to record two consecutive high-magnification images under this beam current, the damage begins to be appreciated. The convergence semi-angle was kept at 17 mrad, while the inner collection angle was  $\approx 10$  mrad. With this configuration the image contrast is less affected by the atomic number, but still heavier elements can be identified as it is shown in Figures 5a and 5b. Trying to corroborate the presence of silver in the form of Ag nanoparticles, Figure 5b was Fourier filtered in order to remove the periodic display; the inverse image of the non-periodic FFT revealed the existence of ca. 3-4 nm Ag nanoparticles (Figure 5c, pointed by red arrows). The fact that some of the silver nanoparticles could become larger than the mesoporous cages of MIL-100, which have been reported to be 25 and 29  $\text{\AA}$ <sup>[20]</sup>, suggests that the Ag may occupy more than one cage. The occupation of the cages may also be confirmed by the lower overall intensity of the XRD profiles, together with the inversion of the 220 and 311 reflections (Figure 4b). In the 10:1 sample the overall profile shows lower intensity as well as a notable increase of the 311 intensity as compared to the parent MIL-100(Fe) suggesting that the pores are being filled or impregnated by the silver salt. Further decrease of the Fe to Ag ratio leads to an excess of silver that tends to agglomerate forming larger crystalline particles outside the MIL-100(Fe) yielding sharp diffraction peaks. The partial fill of the MIL100(Fe) mesocages by Ag species could also be suggested by the appearance of low intense peaks in PSD curves of the Ag-impregnated samples,

right below the main PSD maxima (Figure S2). The nanoparticles formation mechanism could be the result of the diffusion of the molten  $\text{AgNO}_3$  salt in its liquid state through the interior of the porous structure, helped by the presence of some water within the MIL-100(Fe) pores, followed by the auto-reduction of the metal in order to finally grow metal nanoparticles.

In summary,  $C_s$ -corrected STEM HAADF and ADF can be employed to characterize in detail highly beam sensitive materials which present complex topologies as it is the case of MIL-100(Fe) material. By using low-dose techniques, minimizing the beam current and using low exposure times, in combination with an appropriate selection of the electron detectors, the building units of these types of materials can be elucidated. Even, under ADF conditions and low beam current metallic, Ag clusters can be located within the cavities making clear the benefits of electron microscopy methods for the characterization of metal loaded porous frameworks.

The results achieved in this study are of special significance considering the importance of metal nanoparticles loaded onto porous supports in the catalytic field and the relevant role of Ag nanoparticles in biomedical applications and the biocompatible character of the MIL-100(Fe) materials, which can be considered as BioMOF.

## Experimental Section

### Materials synthesis and characterization

MIL-100(Fe) was synthesized at room temperature and in water, following a procedure described elsewhere [5]. A clear solution of trimesic acid (1.676 g, 7.6 mmol) in 23.72 g of 1 M NaOH (22.8 mmol) aqueous solution was added dropwise over another solution formed by 2.26 g (11.4 mmol) of  $\text{FeCl}_2 \cdot 4\text{H}_2\text{O}$  and 97.2 g of water. That addition produces the immediate precipitation of a solid. The mixture, whose molar composition was 1.5 Fe/1.0  $\text{H}_3\text{BTC}$ /3.0 NaOH/880  $\text{H}_2\text{O}$ , was magnetically stirred at room temperature for 24 h. The solid was recovered by centrifugation at 3700 rpm, and then it was washed three times with water and one more time with ethanol, and dried at 70 °C. Finally, the amount of Fe was estimated using thermogravimetric analysis, certifying that the residual sample was pure  $\text{Fe}_2\text{O}_3$ .

Samples Ag@MIL-100(Fe) were prepared with three different Ag loadings calculated from the Fe content of the MIL-100(Fe) and  $\text{AgNO}_3$  using 1:1, 5:1 and 10:1 Fe:Ag. In a typical experiment, for instance 1:1 solid state reaction, 0.201 g of MIL-100(Fe) of brown-orange color and 0.101 g of white powder  $\text{AgNO}_3$  were mixed as solids in a mortar and pestle for a few minutes until the sample becomes visually homogeneous in a light brown color. Then, the samples were heated in a muffle furnace at 150 °C for 12h using a heating ramp of 2 °C/min. After the thermal treatment the recovered samples show a darker-brown color indicating that the silver atoms may be successfully mixed with MIL-100(Fe).

Powder X-ray diffraction patterns were collected using an X-Ray polycrystalline X'Pert Pro PANalytical diffractometer using  $\text{Cu K}\alpha$  radiation ( $\lambda = 1.5406 \text{ \AA}$ ), with accelerating voltage and current of 45 kV and 40 mA, respectively. TG analyses were registered in a PerkinElmer TGA7 instrument from 25 to 900 °C at a heating rate of 20 °C/min under air flow.

### Electron Microscopy observations

Electron microscopy observations were performed using a FEI TITAN XFEG operated at 300 kV. The microscope is equipped with a CEOS spherical aberration corrector for the electron probe which was aligned prior every experiment using a gold standard sample. The typical aberration values obtained were:  $A_1 = 1.10 \text{ nm}$ ;  $A_2 = 12.6 \text{ nm}$ ;  $B_2 = 8.87 \text{ nm}$ ;  $C_3 = 416.4 \text{ nm}$ ;  $A_3 = 663.6 \text{ nm}$ ;  $S_3 = 340.9 \text{ nm}$  assuring a 0.8 Å resolution under normal circumstances. The beam current employed was set between 1 and 2 pA, with total exposure time of 6 seconds.

## Acknowledgements

AM acknowledges the Government of Aragon and the European Social Fund under the project grant number E/26 "Construyendo Europa desde Aragón" 2014-2020. This work has been partially financed by the Spanish State Research Agency (Agencia Española de Investigación, AEI) and the European Regional Development Fund (Fondo Europeo de Desarrollo Regional, FEDER) through Project MAT2016-77496-R (AEI/FEDER, UE).

**Keywords:** Metal-organic framework • Electron Microscopy • Metal Nanoparticles

- [1] (a)O. M. Yaghi, M. O'Keeffe, N. W. Ockwig, H. K. Chae, M. Eddaoudi, J. Kim, *Nature* **2003**, 423, 705–714; (b)G. Ferey, *Chem. Soc. Rev.* **2008**, 37, 191-214.
- [2] (a)N. Stock, S. Biswas, *Chem. Rev.* **2012**, 112, 933-969; (b)M. Sánchez-Sánchez, N. Getachew, K. Díaz, M. Díaz-García, Y. Chebude, I. Díaz, *Green Chem.*, 2015,17, 1500-1509 **2015**, 17, 1500-1509; (c)K. Guesh, C. A. D. Caiuby, A. Mayoral, M. Díaz-García, I. Díaz, M. Sanchez-Sanchez, *Cryst. Growth Des.* **2017**, 17, 1806-1813; (d)M. Díaz-García, A. Mayoral, I. Díaz, M. Sánchez-Sánchez, *Cryst. Growth Des.* **2014**, 14, 2479–2487.

- [3] (a)M. Eddaoudi, J. Kim, N. Rosi, D. Vodak, J. Wachter, M. O’Keeffe, O. M. Yaghi, *Science* **2002**, 295, 469-472; (b)J. Sánchez-Laínez, B. Zornoza, A. Mayoral, A. Berenguer-Murcia, D. Cazorla-Amorós, C. Téllez, J. Coronas, *J. Mater. Chem. A* **2015**, 3, 6549-6556.
- [4] D. Y. Hong, Y. K. Hwang, C. Serre, G. Férey, J. S. Chang, *Adv. Funct. Mater.* **2009**, 19, 1537-1552.
- [5] (a)P. Horcajada, T. Chalati, C. Serre, B. Gillet, C. Sebrie, T. Baati, J. F. Eubank, D. Heurtaux, P. Clayette, C. Kreuz, J. S. Chang, Y. K. Hwang, V. Marsaud, P. N. Bories, L. Cynober, S. Gil, G. Férey, P. Couvreur, R. Gref, *Nat. Mater.* **2010**, 9, 172-178; (b)P. Horcajada, C. Serre, D. Grosso, C. Boissiere, S. Perruchas, C. Sanchez, G. Férey, *Adv. Mater.* **2009**, 21, 1931-1935; (c)P. Horcajada, C. Serre, M. Vallet-Regí, M. Sebban, F. Taulelle, G. Férey, *Angew. Chem. Int. Ed.* **2006**, 45, 5974-5978.
- [6] (a)K. Fujii, A. L. Garay, J. Hill, E. Sbircea, Z. Pan, M. Xu, D. C. Apperley, S. L. James, K. D. M. Harris, *Chem. Commun.* **2010**, 46, 7572-7574; (b)C. Volkringer, T. Loiseau, N. Guillou, G. Férey, E. Elkaïm, A. Vimont, *Dalton Trans.* **2009**, 2241-2249.
- [7] Z. Fang, B. Bueken, D. E. D. Vos, R. A. Fischer, *Angew. Chem. Int. Ed.* **2015**, 54, 7234-7254.
- [8] (a)A. Mayoral, L. F. Allard, D. Ferrer, R. Esparza, M. Jose-Yacaman, *J. Mater. Chem.* **2010**, 21, 893-898; (b)R. Pérez-Hernández, A. Gutiérrez-Martínez, A. Mayoral, F. L. Deepak, M. E. Fernández-García, G. Mondragón-Galicia, M. Miki, M. José-Yacamán, *Adv. Mater. Res.* **2010**, 132, 205-219; (c)A. Mayoral, J. Coronas, C. Casado, C. Tellez, I. Díaz, *Chem. Cat. Chem.* **2013**, 5, 2595-2598.
- [9] (a)M. Haider, S. Uhlemann, E. Schwan, H. Rose, B. Kabius, K. Urban, *Nature* **1998**, 392, 768-769; (b)P. E. Baston, N. Dellby, O. L. Krivanek, *Nature* **2002**, 418, 617-620.
- [10] (a)Z. Y. Li, N. P. Young, M. D. Vece, S. Palomba, R. E. Palmer, A. L. Bleloch, B. C. Curley, R. L. Johnston, J. Jiang, J. Yuan, *Nature* **2008**, 451, 46-48; (b)A. Mayoral, D. A. Blom, M. M. Mariscal, C. Guitierrez-Wing, J. Aspiazua, M. Jose-Yacaman, *Chem. Commun.* **2010**, 46, 8758-8760; (c)H. Yang, Y. Wang, X. Chen, X. Zhao, L. Gu, H. Huang, J. Yan, C. Xu, G. Li, J. Wu, A. J. Edwards, B. Dittrich, Z. Tang, D. Wang, L. Lehtovaara, H. Häkkinen, N. Zheng, *Nat. Commun.* **2016**, 7, 12809; (d)M. Castrillon, A. Mayoral, C. Magen, J. G. Meier, C. Marquina, S. Irusta, J. Santamaria, *Nanotechnology* **2012**, 23, 085601-085610.
- [11] A. Mayoral, Y. Sakamoto, I. Diaz, *Zeolites and Mesoporous Crystals Under the Electron Microscope* Springer, Switzerland, **2015**.
- [12] (a)A. Mayoral, R. Arenal, V. Gascon, C. Marquez-Alvarez, R. M. Blanco, I. Diaz, *Chem. Cat. Chem* **2013**, 5, 903-909; (b)A. Mayoral, R. M. Blanco, I. Diaz, *J. Mol. Catal. B: Enzym* **2013**, 90, 23-25.
- [13] C. Wiktor, S. Turner, D. Zacher, R. A. Fischer, G. V. Tendeloo, *Microporous Mesoporous Mater.* **2012**, 162, 131-135.
- [14] (a)A. Mayoral, T. Carey, P. A. Anderson, I. Diaz, *Micropor. Mesopor. Mater.* **2013**, 166, 117-122; (b)A. Mayoral, J. E. Readman, P. A. Anderson, *J. Phys. Chem. C* **2013**, 117, 24485-24489.
- [15] (a)A. Mayoral, M. Sanchez-Sanchez, A. Alfayate, J. Perez-Pariente, I. Diaz, *Chem. Cat. Chem.* **2015**, 7, 3719-3724; (b)A. Mayoral, J. G. Ming, S. B. Hong, *Microporous Mesoporous Mater.* **2016**, 2016, 129-133.
- [16] A. Mayoral, R. M. Hall, R. Jackowska, J. E. Readman, *Angew. Chem. Int. Ed.* **2016**, 55, 16127-16131.
- [17] (a)M. Meledina, S. Turner, M. Filippousi, K. Leus, I. Lobato, R. K. Ramachandran, J. Dendooven, C. Detavernier, P. V. D. Voort, G. V. Tendeloo, *Part. Part. Syst. Character.* **2016**, 33, 382-387; (b)Y. Zhu, J. Ciston, B. Zheng, X. Miao, C. Czarnik, Y. Pan, R. Sougrat, Z. Lai, C. E. Hsiung, K. Yao, I. Pinnau, M. Pan, Y. Han, *Nat. Mater.* **2017**, 16, 532-536; (c)H. Deng, S. Grunder, K. E. Cordova, C. Valente, H. Furukawa, M. Hmadeh, F. Gandara, A. C. Whalley, Z. Liu, S. Asahina, H. Kazumori, M. O’Keeffe, O. Terasaki, J. F. Stoddart, O. M. Yaghi, *Science* **2012**, 336, 1018-1023.
- [18] (a)Q. L. Zhu, J. Li, Q. Xu, *J. Am. Chem. Soc.* **2013**, 135, 10210-10213; (b)A. Aijaz, A. Karkamkar, Y. J. Choi, N. Tsumori, E. Rönnebro, T. Autrey, H. Shioyama, Q. Xu, *J. Am. Chem. Soc.* **2012**, 134, 13926-13929.
- [19] A. Corma, P. Concepcion, M. Boronat, M. J. Sabater, J. Navas, M. Jose-Yacaman, E. Larios, A. Posadas, M. A. Lopez-Quintela, D. Buceta, E. Mendoza, G. Guilera, A. Mayoral, *Nat. Chem.* **2013**, 5, 775-781.
- [20] P. Horcajada, S. Surblé, C. Serre, D. Y. Hong, Y. K. Seo, J. S. Chang, J. M. Grenèche, I. Margiolaki, G. Férey, *Chem. Commun.* **2017**, 2820-2822.
- [21] A. Turrina, R. Garcia, A. E. Watts, H. F. Greer, J. Bradley, W. Zhou, P. A. Cox, M. D. Shannon, A. Mayoral, J. L. Casci, P. A. Wright, *Chem. Mater.* **2017**, 29, 2180-2190.
- [22] S. Hovmöller, *Ultramicroscopy* **1992**, 41, 121-135.
- [23] (a)S. Keskin, S. Kızılel, *Ind. Eng. Chem. Res.* **2011**, 50, 1799-1812; (b)B. Kwakye-Awuah, C. Williams, M. A. Kenward, I. Radecka, *J. Appl. Microbiology* **2008**, 104, 1516-1524.
- [24] A. Mayoral, P. A. Anderson, *Nanotechnology* **2007**, 18, 165708.
- [25] Y. P. Wu, G. Wang, W. W. Dong, J. Zhao, D. S. Li, J. Zhang, X. Bu, *Inorg. Chem.* **2017**, 56, 1402-1411.

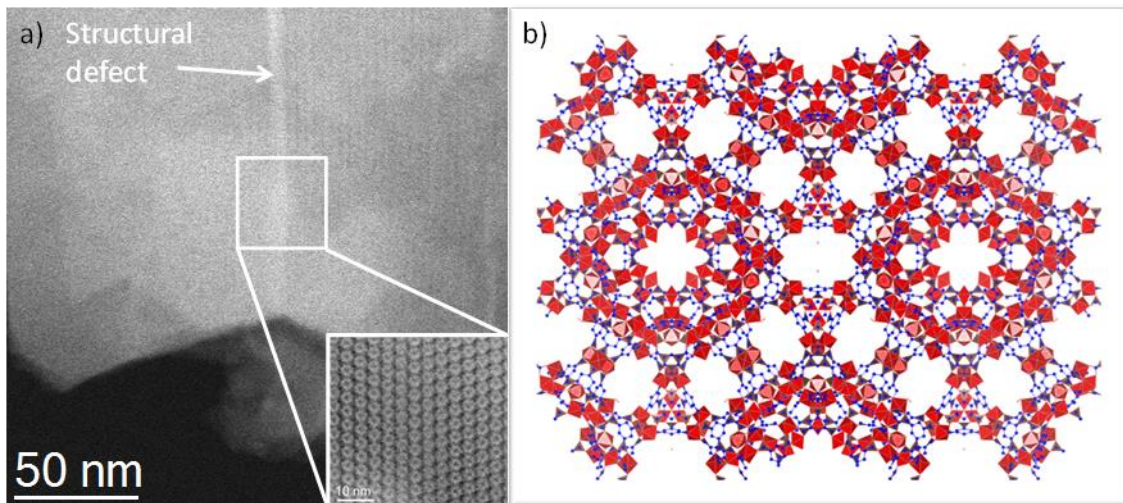


**Figure 1.** Low-magnification  $C_s$ -corrected STEM-HAADF image of MIL-100(Fe), where a twin plane defect is marked by a white arrow. A closer look of the twin boundary is shown inset. b) Schematic representation of the structure orientated along the [110], in red the Fe octahedra and in blue the C linkers.

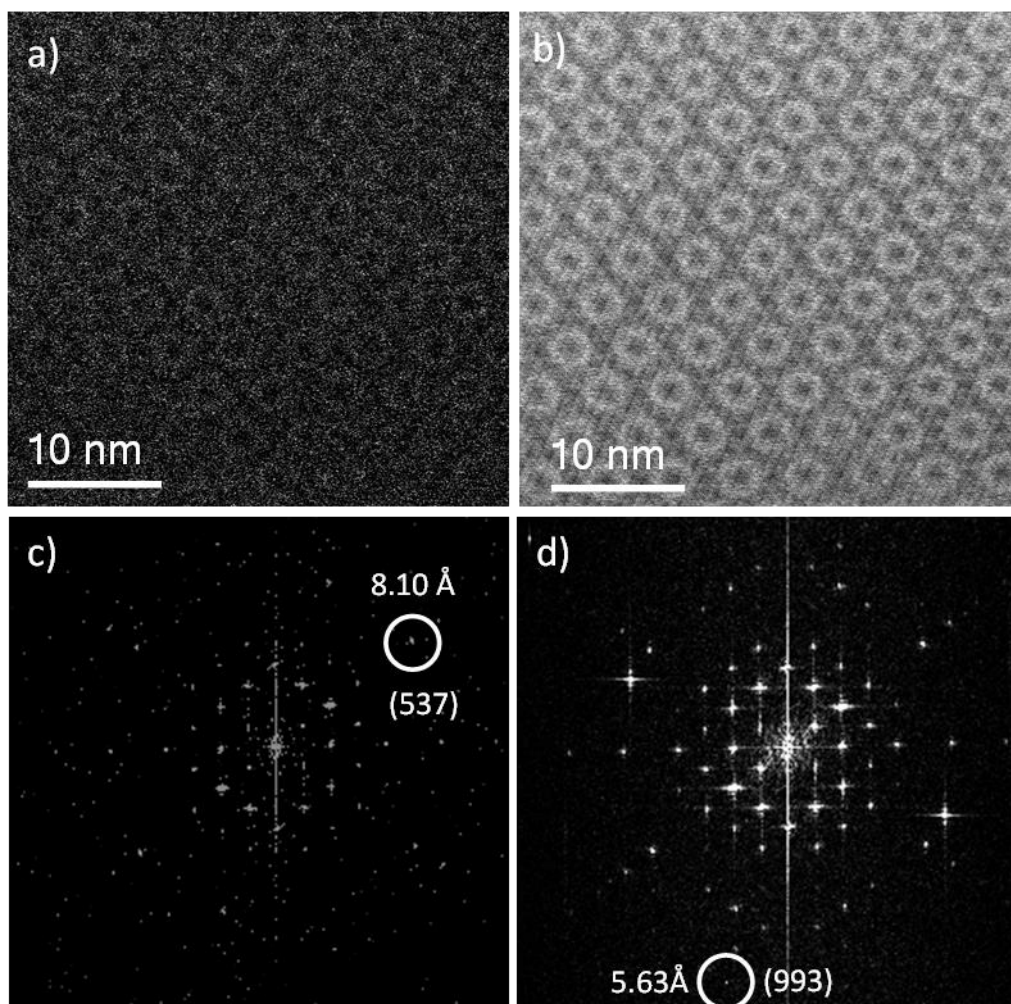


**Figure 2.**  $C_s$ -corrected STEM images of MIL-100(Fe). a) Using pure HAADF conditions; b) ADF conditions. c) and d) FFT patterns of the HAADF and ADF images respectively.

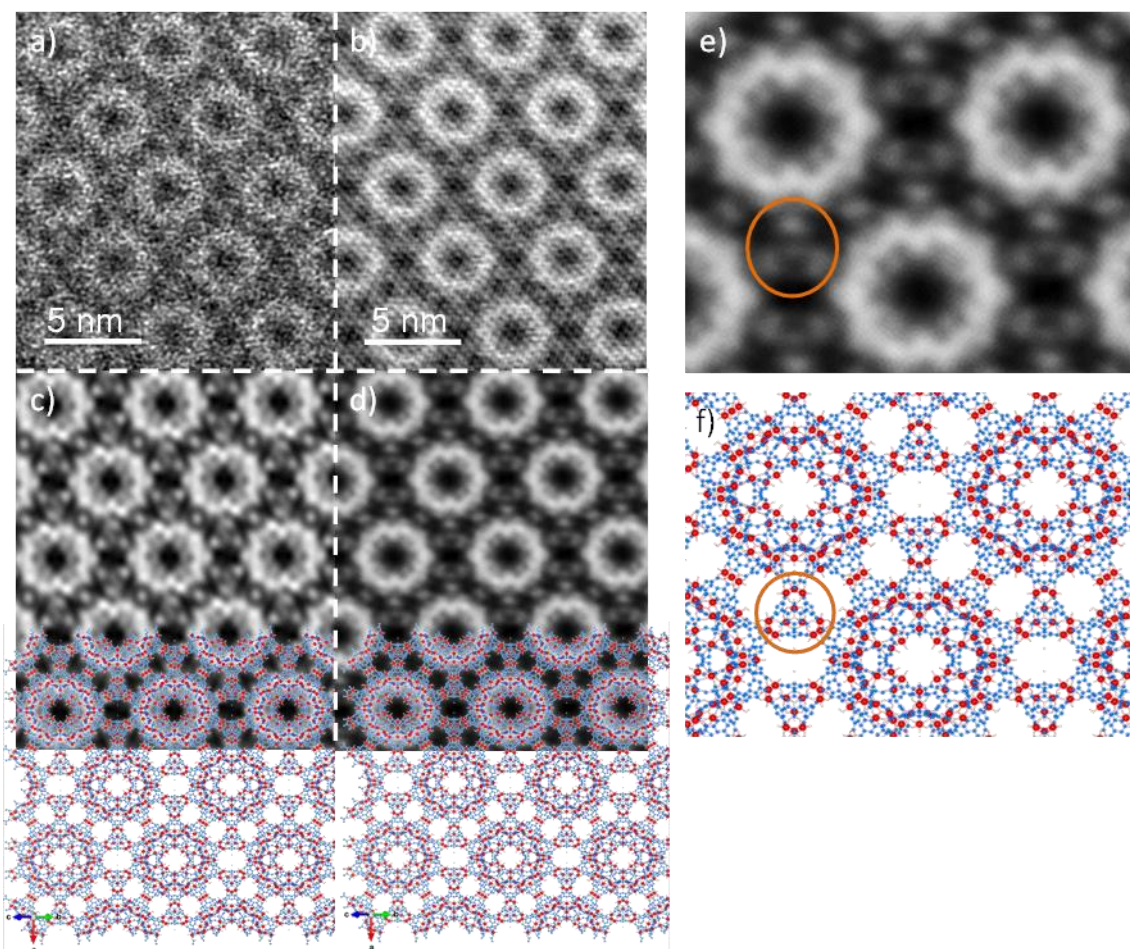


**Figure 3.** Experimental  $C_c$ -corrected STEM images recorded along the  $[110]$  orientation. a) HAADF FFT filtered image. b) FFT filtered ADF image of the same crystal region. c) Electronic potential map obtained from the raw HAADF image. d) Electronic potential map obtained from the raw ADF image. In both cases the MIL-100(Fe) model has been superimposed. e) Closer observation of the MIL-100(Fe) structure obtained from figure 3d. The orange circle indicates the supertetrahedra forming the cavities. The signals in the corner of the projected triangle correspond to 3 Fe cations. f) MIL-100(Fe) model showing the same units as presented in figure 3e.

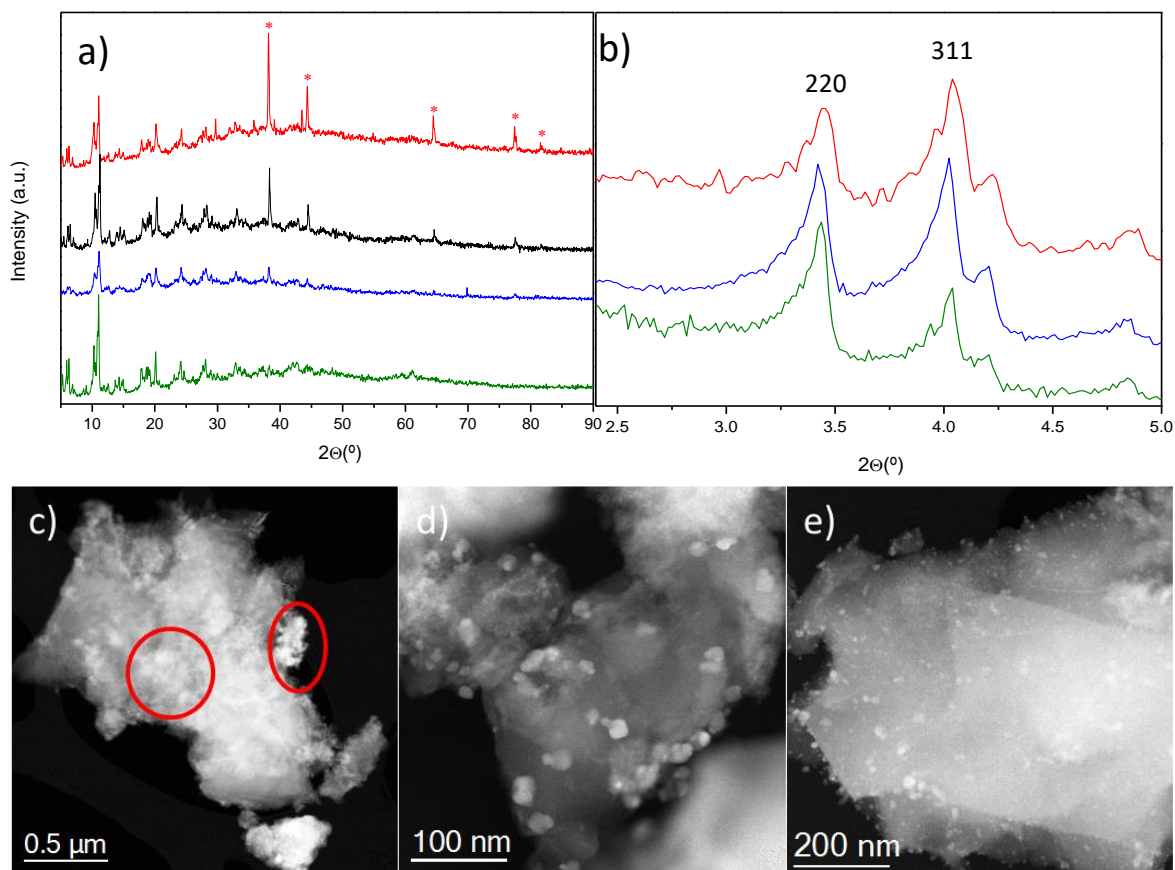


**Figure 4.** a) Powder XRD diffractograms of 1:1 (red); 5:1 (black); 10:1 (blue) Fe:Ag, as well as the parent MIL-100(green). The diffractions peaks marked with an asterisk correspond to  $\text{Ag}^0$ . b), c) and d)  $C_s$ -corrected STEM-HAADF images of 1:1; 5:1 and 10:1 Fe:Ag.

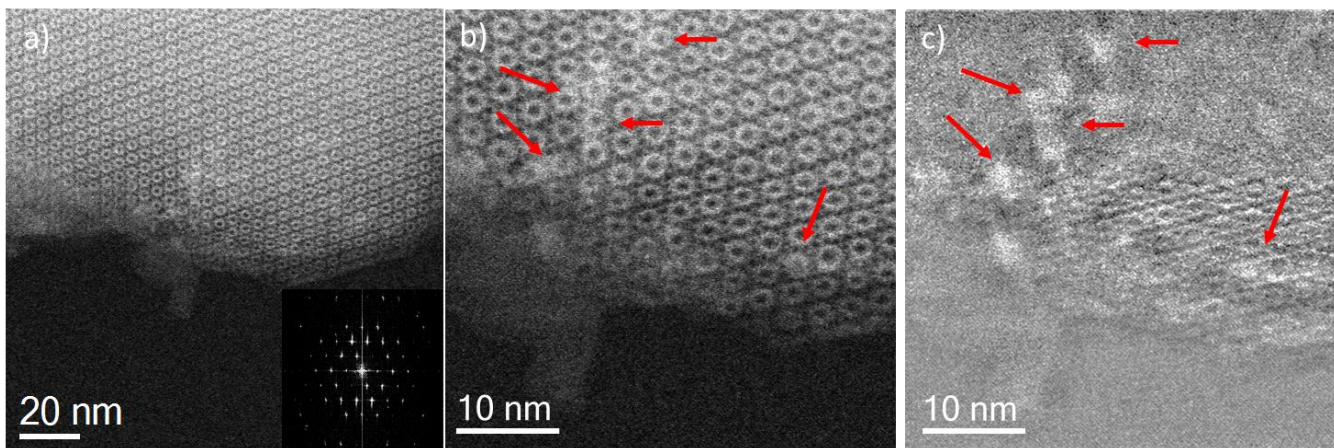


**Figure 5.** a)  $C_s$ -corrected STEM-ADF images of silver loaded MIL-100(Fe). a) High-magnification image of the porous structure, with the FFT diffractograms shown inset. b) Closer observation of the MIL-100(Fe) with the features with stronger contrast are pointed by red arrows. c) FFT filtered image with the periodic arrangement removed for a better visualization of the Ag particles.